\$ SUPER

Contents lists available at ScienceDirect

Engineering Geology

journal homepage: www.elsevier.com/locate/enggeo



Experimental investigation on the formation and failure of landslide dams considering the landslide mobility and river flow

Hongwei Luo ^{a,b}, Gordon G.D. Zhou ^{a,b,c,*}, Xueqiang Lu ^{a,b}, Kahlil F.E. Cui ^{a,b}, Yuting Zhao ^a, Yunxu Xie ^{a,b}, Wei Zhong ^{a,b}, Jiawen Zhou ^d, Alessandro Pasuto ^e

- ^a Key Laboratory of Mountain Hazards and Engineering Resiliences / Institute of Mountain Hazards and Environment, Chinese Academy of Sciences, Chengdu 610000, China
- ^b University of Chinese Academy of Sciences, Beijing 100000, China
- ^c China-Pakistan Joint Research Center on Earth Sciences, CAS-HEC, Islamabad, Pakistan
- ^d State Key Laboratory of Hydraulics and Mountain River Engineering, Sichuan University, Chengdu 610065, China
- e National Research Council-Research Institute for Geo-Hydrological Protection (CNR-IRPI), Padova 35127, Italy

ARTICLE INFO

Keywords: Landslide River blockage Froude number Landslide dam Dam faliure Erosion rate

ABSTRACT

River blockage by landslides is a common geological disaster in mountainous regions that threaten the safety of human lives. Therefore, it is necessary to better understand the formation and failure of landslide dams. In this work, flume experiments are conducted to study the influence of landslide mobility and river flow dynamics, both characterized by the Froude number, on the formation process of landslide dams and the degree of river blockage. Here, river blockage is classified as either complete or partial depending on the ratio between the minimum dam height over the river flow depth. A criterion based on the relative Froude numbers of landslides and rivers is proposed to judge the degree of river blockage. We further found that during breaching, the erosion rate is still mainly controlled by the Froude number of the breaching flood and less so by the degree of blockage. The results of this work are expected to enhance the understanding of the formation and failure of landslide dams.

1. Introduction

The formation and failure of landslide dams are common geological disasters in mountainous regions (Costa and Schuster, 1988; Coussot and Meunier, 1996; Xu et al., 2009; Fan et al., 2020; Luo et al., 2022). The water level behind these natural dams rise over time, eventually breaching the crest which result in further structural failure and outburst flooding (Cui et al., 2009; Fan et al., 2019; Jin et al., 2022; Zhou et al., 2022a). Landslide dam failure releases massive amounts of water and soils over a short period of time, posing a great threat to communities and infrastructure downstream (Korup, 2002; Ermini and Casagli, 2003; Tacconi Stefanelli et al., 2016; Zhong et al., 2021; Shi et al., 2023). One such event is the Tangjiashan landslide dam induced by the 2008 Wenchuan Earthquake, in which the impounded river formed a huge dammed lake which threatened more than 2.5 million people downstream (Dong et al., 2011; Peng and Zhang, 2011; Fan et al., 2012; Xu et al., 2013). It is therefore important to better understand the formation

process of landslide dams and the mechanisms that control their failure to further support the related hazard prevention and mitigation.

When landslides rush into rivers, some of the landslide material can be immediately carried away by the river's flow. Consequently, the shape of the landslide dam and the extent of the river blockage are influenced by the landslide's mobility and the river's dynamics. Consider two landslides of equal volume but different velocities entering the same river. A slow-moving landslide's momentum can be easily counteracted by the river's flow, making it more likely to be redirected along the river's course. This redirection may prevent the landslide from reaching the opposite bank, resulting in only a partial blockage of the river (Costa and Schuster, 1988). After the landslide material settles, water can continue to flow through the unblocked sections of the river (Fig. 1a and b) (Liao et al., 2019; Nian et al., 2021). In contrast, a fast-moving landslide's momentum can easily overcome the river's flow, allowing it to reach the opposite bank and completely block the river (Fig. 1c and d) (Xu et al., 2013; Luo et al., 2022; Zeng et al., 2022). This

E-mail address: gordon@imde.ac.cn (G.G.D. Zhou).

^{*} Corresponding author at: Key Laboratory of Mountain Hazards and Engineering Resiliences / Institute of Mountain Hazards and Environment, Chinese Academy of Sciences, Chengdu 610000, China.

creates a natural dam that impounds the river's flow, which may later be released as outburst floods. These processes illustrate that both the extent of river blockage (formation of landslide dams) and subsequent dam breach modes are influenced by the interaction between landslide mobility and river flow dynamics (Schuster, 1986; Chen et al., 2015; Shi et al., 2022).

The influence of river dynamics on landslide dam formation is significant but is often ignored in existing landslide dam studies, e.g. Xu et al. (2013); Zhou et al. (2019b); Li et al. (2020a). Recent studies incorporated the influence of rivers on landslide dam formation, but usually assume constant discharges, ignoring the influence of variable water flow rate on landslide dam formation and river blockage (Liao et al., 2019; Luo et al., 2022; Zhu et al., 2023). Nian et al. (2020) and Jin et al. (2022) considered the influence of landslide discharge and water flow rate on the degree of river blockage. Flow regimes impact the formation of landslide dams, especially the deposit height (Liao et al., 2019), but are not clearly reflected by the discharge since a single discharge value can correspond to several flow regimes. Landslide and river flows are driven by gravitational forces, and the interaction between them is strongly influenced by changes in their momentum (inertial forces) (Choi et al., 2015). Dimensionless quantities, such as the Froude number (the ratio of inertial forces to gravitational forces), can be used to characterize both the landslide and river flow regimes and at the same time can be used as a parameter for determining degree of river

The degree of river blockage can influence the erosion mechanism during dam breach (Swanson et al., 1986; Liao et al., 2019; Zhou et al., 2022a). When the river is partially blocked by small-scale landslides with low mobility, lateral erosion is the primary erosion mechanism as river flow can pass by or through the deposit without interruption (Fig. 1a and b). However, when a large-scale landslide with high mobility completely blocks a river channel, the upstream inflow level has to gradually rise to flow over the landslide dam (Fig. 1c and d); in this condition, the erosion mechanism of the large-scale landslide dam by the outburst flood includes both lateral and longitudinal erosion (Zhang et al., 2021; Shi et al., 2022). Although large-scale landslide dams are considered more threatening and have been the primary focus of research on the dam failure and erosion, partial and complete blockages by relatively small-scale landslide dams occur more frequently and thus deserve to be understood more clearly (Ermini and Casagli, 2003; Fan et al., 2012; Fan et al., 2020; Takayama and Imaizumi, 2022). Therefore, it is necessary to investigate the dam failure and erosion processes of small-scale landslide dams that cause partial or complete river blockage.

In this study, we conduct flume experiments to investigate the conditions that lead to the complete or partial damming of rivers by landslides and the failure mechanisms corresponding to these modes of

blockage. The tests are intended to (i) relate the degree of river blockage, i.e. extent of redirection and deposition height, to the river flow dynamics and landslide mobility, (ii) propose a method to determine whether a river can be completely or partially dammed by a landslide only on the base of landslide mobility and river flow dynamics quantified by using the Froude number, and (iii) investigate the relationship between the flow regimes of the outburst flood and the lateral erosion rate of the landslide dam. Results from this work are expected to enhance the comprehension of river blockage mechanisms and introduces a novel method for early identification of landslide dam formation and breaching.

2. Experimental method

2.1. Experimental set-up and materials

The experiments are conducted at the Dongchuan Debris Flow Observation and Research Station (DDFORS), Dongchuan District, Kunming City, Yunnan Province, China (N26°14', E103°08'). The experimental apparatus (Fig. 2) is composed of two channels that are welded perpendicular to each other. One channel, here referred to as Channel No. 1, is an inclined flume in which granular materials are released. Channel No. 1 is 0.20 m wide, 3.40 m long, and 0.40 m deep, and is constantly inclined at $\theta = 40^{\circ}$ (Fig. 2a). Landslide are stored and released from pluggable gates that can be installed at three different locations along Channel No. 1. Altering the initial locations of the landslide mass L = [1.5, 2.1, 2.7] m (the distance from the end of Channel No. 1) is done to achieve different landslide velocities. Channel No. 2 is positioned perpendicular to Channel No. 1 and serves as a modeled river. This section is 4.45 m long, 0.40 m wide, and 0.40 m deep (Fig. 2b). Channel No. 2 is wider than Channel No. 1 in order to facilitate a clear observation of the river blockage by landsliding. For the same reason, sidewalls are set perpendicular to the ground instead of being inclined at an angle which are more akin to natural gully geometries. Clearwater is pumped into Channel No. 2 from a water tank and the inflow rate is adjusted by increasing or decreasing the number of water pumps. The water inlet is 0.70 m away from the intersection of the two channels and an energy dissipation net is positioned 0.20 m from the inlet to minimize turbulence (Fig. 2a).

Four digital video cameras (SONY FDR-AX40, 1440×1080 pixels, 25 fps) are used to monitor the experiment. Camera#1 is installed at the outlet of Channel No. 2 to obtain a cross-sectional view of the landslide moving into the river and the subsequent dam formation. Camera#1 also records the width change of the breached section of the dam over time. Camera#2, positioned at the side of Channel No. 2 and focuses on the intersection with Channel No. 1, primarily captures the water flow depth and the motion of tracer particles that are put into the water flow

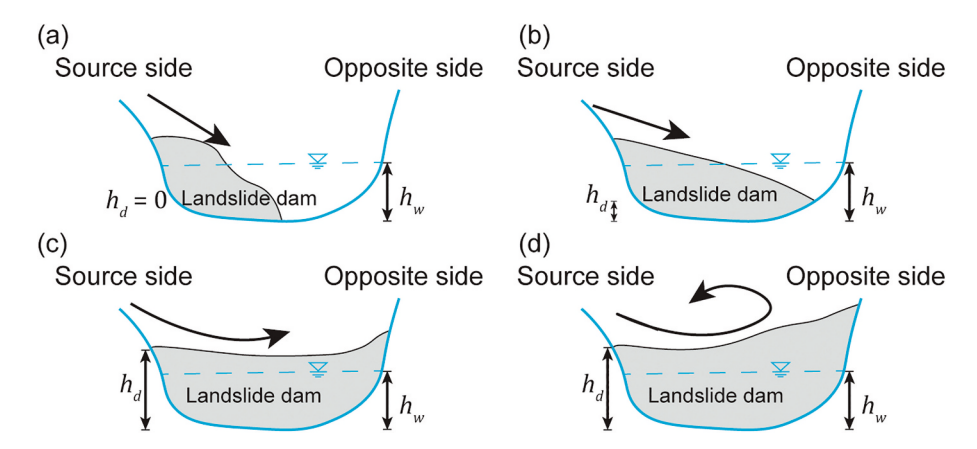


Fig. 1. The two types of river blockages by landslide identified based on the relationship between the minimum deposit height h_d and water depth h_w : (a) and (b) are partial blockage scenarios; (c) and (d) are the completely blocked scenarios.

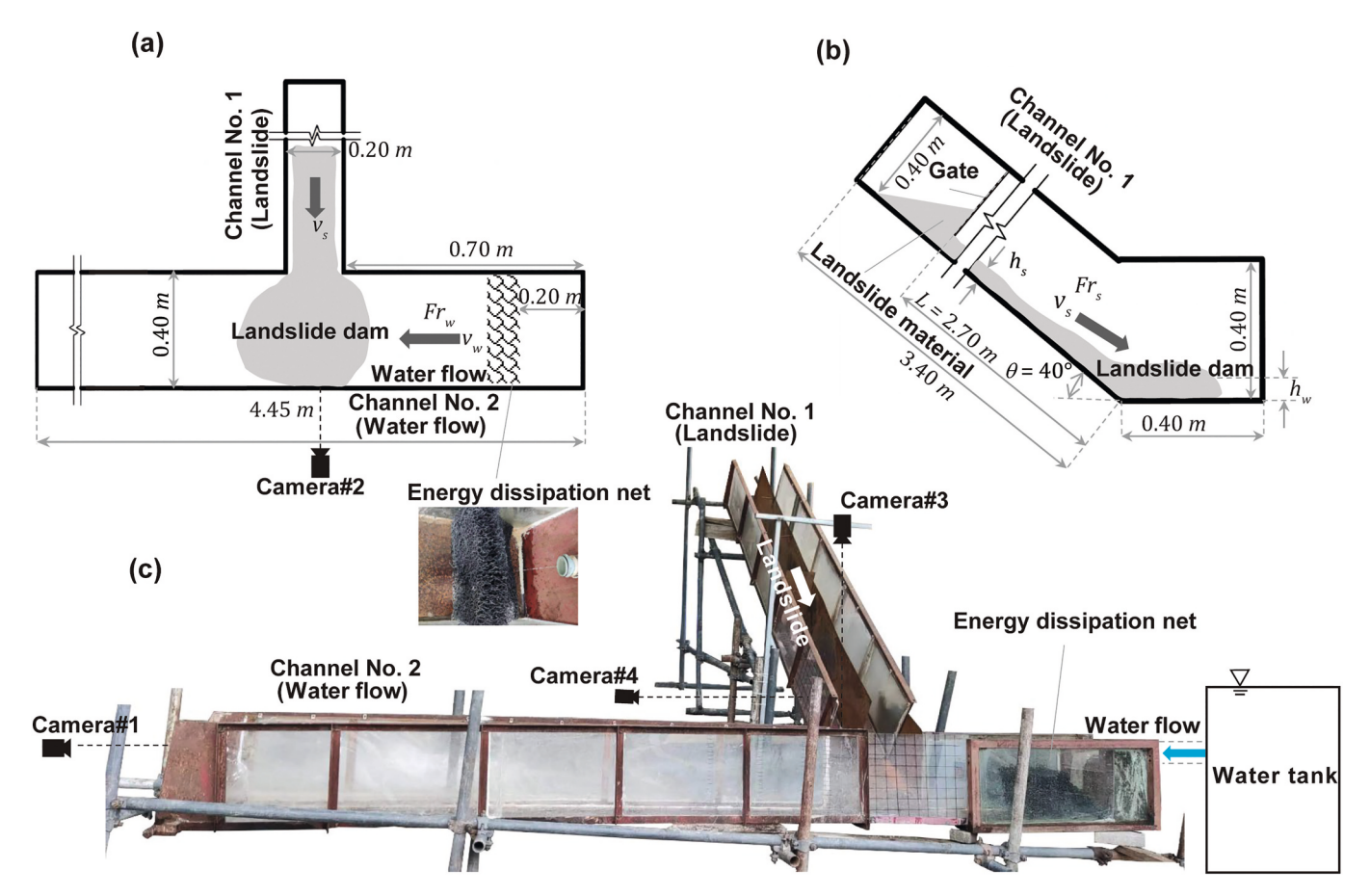


Fig. 2. Schematic diagram of the set-up as seen (a) from the top and (b) from the side. (c) Real photo of the set-up and the positions of the cameras.

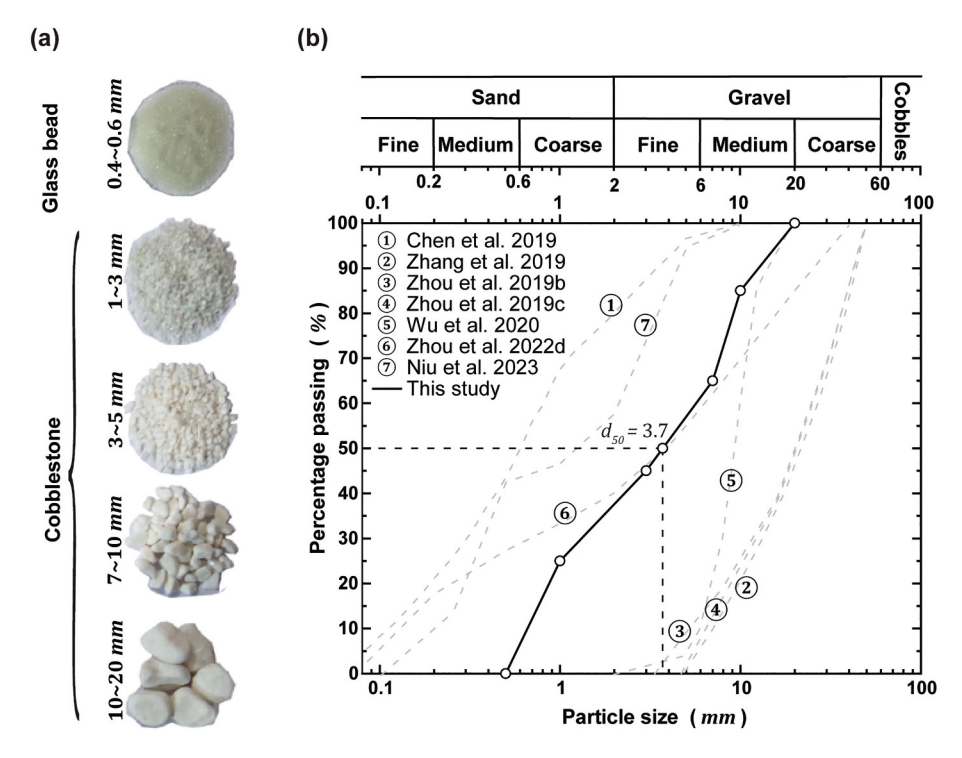


Fig. 3. (a) The landslide material used in this paper (Hu et al., 2020), (b) Particle size distribution of the granular flow material (solid line). The dashed lines are particle size distributions obtained from the literatures for comparison (Chen et al., 2019; Niu et al., 2023; Wu et al., 2020; Zhang et al., 2019; Zhou et al., 2019b,c; Zhou et al., 2022d).

when the river is stable. Camera#3 is installed above the confluence of the two channels to obtain a top view of the landslide intrusion and river blockage. Camera#4 is installed beside Channel No. 1 to record the landslide movement along the chute (Fig. 2a and c), from which measurements of its flow height and velocity are obtained. The formation of landslide dam and subsequent failure are observed through transparent plexiglass walls. Grids are drawn over the glass sidewalls to facilitate measurement of the velocity and depth of the landslide and river flow (Fig. 2c). To reduce the perspective distortion caused by the camera, we placed the camera as close as possible to the gridded side wall.

The landslide materials used in the experiments are mixtures of 0.4 \sim 0.6 mm glass beads and non-uniformly sized pebbles that represent the fine debris and granular materials in landslides, respectively (Fig. 3a). The color contrast of these materials with water allows for clear observation of the formation and failure process of the landslide dam. The landslide materials are thoroughly dried before each experiment to eliminate the influence of moisture. The weight, composition, and size distribution of the landslide materials are held constant in all test cases. Fig. 3b shows the grain size distribution of the landslide material used in the experiment. Where the maximum diameter is 20 mm and the median particle size d_{50} is 3.70 mm. The grain density ρ_h is 2747 kg/m^3 and the interface friction angle α between the landslide materials and the bed of both channels is 33.5° (Hu et al., 2020). Each test uses a total material volume of $0.016 \, m^3$. Evenly mixed granular materials are poured into Channel No. 1 behind the sluice gate. Upon initiating the experiments, the water pump and cameras are activated. After the water flow stabilizes, the sluice gate is rapidly opened, allowing particles to flow down Channel No. 1 and subsequently block Channel No. 2, forming the landslide dam.

2.2. Test design

The degree of river blockage is related to the flow regime of the landslide and river. To compare the landslide mobility and river flow dynamics, the Froude number is used:

$$Fr_{s(w)} = \frac{v_{s(w)}}{\sqrt{gh_{s(w)}cos\theta}} \tag{1}$$

where v and h are the landslide and river flow velocities, g is the acceleration due to gravity $(9.8 \ m/s^2)$, and θ is the slope angle. The subscripts s and w denote that the quantities are for the landslide and the river respectively. The velocities of the landslide and water flow are determined by tracking tracer particles floating on their surfaces, while

their flowing depths are obtained by analyzing the snapshots from the sidewalls recorded by Cameras#2 and 4.

Each test set-up is characterized by a combination of Fr_s and Fr_w . As mentioned in Section 2.1, Fr_s is varied by adjusting the release height of the landslide, and ranges between 5.27 and 6.85. The Fr_w is varied by adjusting the water inflow rate between Q = [0, 2, 2.9, 4.1, 5.1, 6.1]L/s which corresponds to river flow Froude numbers from 1.11 to 1.76. A test case where Q = 0 L/s serves as reference case. This method ensures comparability of flow rates by measuring the surface flow velocity of the fluid before interaction. The test set-up, and the Froude numbers of both the landslide and the river flow are summarized in Table 1. Note that all the Fr_s and most of Fr_w values used here fall within the range of values found in the literature for landslide $(0.5 \sim 15.8)$ (Cui et al., 2015; Chen et al., 2021b; Cheng et al., 2022) and river flows $(0 \sim 1.5)$ (Seip, 2004). Furthermore, representative cases were chosen in the results section to clearly demonstrate the phenomena and highlight the features measured, with no particular reason for their selection.

2.3. The breach discharge measurement of landslide dam failure

After the landslide deposits in the river, the upstream water level gradually rises due to continuous inflow. Dam breach and erosion occurs when the water level exceeds the height of the dam. In this work, we focus on the lateral erosion, since the deposit height is small making it difficult to observe and accurately measure erosion along direction of vertical riverbed (longitudinal erosion). Fig. 4a shows the typical erosion process of a landslide dam and Fig. 4b is a schematic diagram illustrating the lateral erosion of a landslide dam by outburst flood, where e_w represents the lateral erosion rate. The change in the river width is measured from the cross-sectional outlines of the deposit. The velocity of water flow during dam breaching can be calculated through changes in the breach discharge and the cross-sectional area of the dam breach. The outburst discharge can be calculated as:

$$Q_b = \Delta V_b / \Delta t \tag{2}$$

where ΔV_b is the volume of the burst flood in fixed time; Δt is a fixed time interval. Since the flume side walls are made up of smooth plexi-glass, sidewall friction is minimized.

Fig. 4c illustrates the volume change of the dammed lake over Δt with the failure of the landslide dam. To make the measurement of ΔV_b more accurate, the volume of dammed lake is designated into two parts (Part A and Part B) approximated as two geometric shapes (Fig. 4c). Part A is calculated as the product of the distance of the water inlet to the

Table 1 Test program.

Test ID	$L \ (m)$	$Q \ (L/s)$	(m/s)	$\frac{v_w}{(m/s)}$	$h_s imes 10^{-2} \ (m)$	$h_{\rm w} imes 10^{-2} \ (m)$	$h_d imes 10^{-2} \ (m)$	Fr_w	Fr_s	Fr_s/Fr_w	Type
A-1	1.5	0	2.30	-	2.50	_	5.60	_	5.31	_	-
A-2	Group-A	2.00	2.30	0.52	2.50	2.00	6.80	1.17	5.31	4.53	CB
A-3	•	2.90	2.50	0.57	3.00	1.90	1.50	1.32	5.27	3.99	PB
A-4		4.10	2.50	0.78	2.80	2.60	2.50	1.55	5.45	3.52	PB
A-5		5.10	2.30	0.74	2.50	2.90	0.60	1.38	5.31	3.85	PB
A-6		6.10	2.50	0.92	2.70	3.20	0.60	1.64	5.55	3.38	PB
B-1	2.1	0	2.50	_	2.50	-	10.00	_	5.77	_	_
B-2	Group-B	2.00	2.75	0.48	2.59	1.90	6.80	1.11	6.23	6.61	CB
B-3	A	2.90	2.77	0.57	2.80	1.90	8.80	1.32	6.04	4.58	CB
B-4		4.10	2.77	0.78	2.60	2.60	6.30	1.55	6.27	4.05	CB
B-5		5.10	2.77	0.78	2.50	2.90	7.50	1.46	6.39	4.37	CB
B-6		6.10	2.78	0.92	2.50	3.10	6.80	1.67	6.41	3.84	CB
C-1	2.7	0	3.13	_	3.00	-	10.00	_	6.58	_	_
C-2	Group-C	2.00	3.25	0.52	3.00	1.90	10.00	1.21	6.85	5.66	CB
C-3		2.90	3.25	0.63	3.00	2.40	11.30	1.29	6.85	5.31	CB
C-4		4.10	3.16	0.71	2.90	2.60	10.80	1.41	6.77	4.80	CB
C-5		5.10	3.33	0.89	2.50	2.90	6.30	1.67	6.72	4.02	CB
C-6		6.10	3.50	1.00	2.70	3.30	7.40	1.76	6.80	3.86	CB

CB is complete blocked; PB is partial blocked.

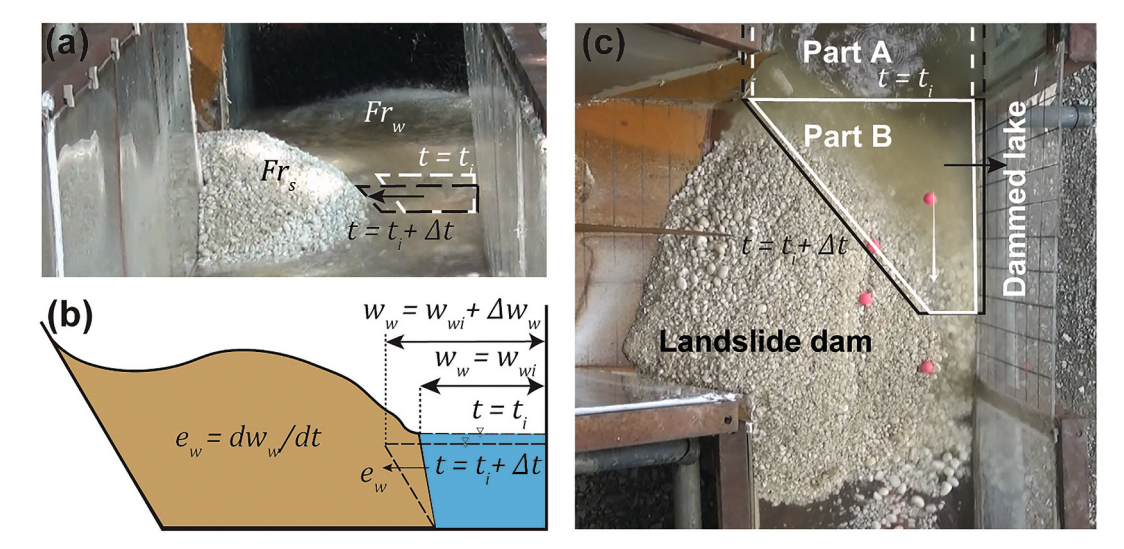


Fig. 4. Schematic diagram of the change of breach width and the calculation of volume: (a) the change of the dam width. (b) Schematic diagram of how lateral erosion rate is calculated; (c) a calculation method of water volume in dammed lake.

junction of the two channels (0.7 m), the width of Channel No. 2 (0.4 m), and the depth-change of the dammed lake (Δh_r) ; the formula is $\Delta V = 0.28\Delta h_r$. The water volume in the Part B is calculated as a trapezoidal prism. The breach width is measured using Camera#1, while the breach depth is determined using Camera#2. The cross-sectional area of the landslide dam breach is modeled as a rectangular area, as only the width of the water surface is measurable in this experiment. This area is calculated as the product of the breach width and the depth of the breach flood. The velocity of the outburst flood is derived by dividing the breach discharge (Q_h) by the area of the breach.

3. Results

3.1. Landslide dam formation

Fig. 5a-c depicts the schematic diagram and the evolution of the upstream depth of the dammed water (h_u/h_w) for an example case B-3 with dimensionless time $(t^*=t/\sqrt{h_w/g})$. The error bars are standard deviations of measurements made over a small observation time window. Here, both the dammed water level height (h_u) and time (t) are scaled by the initial water flow depth (h_w) at t=0. The blockage process can be designated into stages according to steep change in the river flow hydrograph. The first stage involves the downslope flow of the landslide material, its flux into the flowing river and its termination on the opposite side of Channel No. 2. As the landslide rushes into river, the

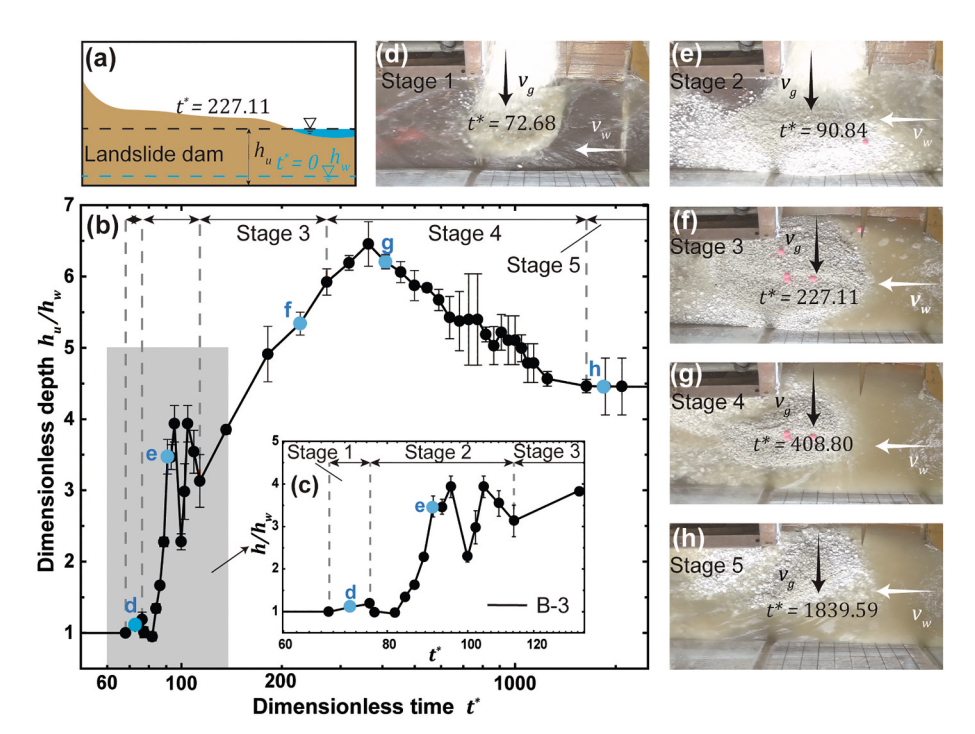


Fig. 5. The upstream water level change of the river with time of an example case B-3. (a) The schematic diagram for the water level change. (b) The evolution of the upstream dimensionless dammed water depth of sample case B-3 in dimensionless time. (c) A closer look at the hydrograph in Stages 1–3. (d-h) Snapshots of the different stages took by the Camera#3. The black and white arrows indicate the flow direction of the landslide and water flow velocities, respectively.

water deflects the landslide along the direction of the flow, resulting in a skewed deposition (Fig. 5d, $t^*=72.68$). In the second stage the landslide material completely deposits into a static granular pile in Channel No. 2 (Fig. 5e, $t^*=90.84$). The oscillations observed in this stage are from the waves of incoming water that are blocked by the dam. In the third stage, the landslide dam is completely formed (Fig. 5f, $t^*=227.11$) and impounds the incoming water flow. The depth of dammed water steadily rises until it reaches the minimum height of the landslide dam.

Dam breaching and failure occurs in the fourth stage (Fig. 5g, $t^*=408.80$). While the breaching flood erodes the landslide dam, the dimensionless depth of dammed water level continues to rise for a short time until the outflow discharge becomes greater than the inflow, at which point the dimensionless depth of dammed water diminishes. In the fifth stage (Fig. 5h, $t^*=1839.59$), the dimensionless depth of dammed water is stable and the resulting morphology of the dam sediment is unchanged. The river flows as it did before the blockage; however, the landslide deposit that have not been washed away completely, results in a more uneven riverbed, permanently raising the upstream water level. This feature indicates that river blockage by landslides does not only influence river morphology over short periods (outburst floods), but can also permanently alter its shape. The above five stages only occur when the river can be completely blocked by landslide.

When most of the landslide material cannot span the entire width of Channel No. 2 (Fig. 6a), the river is considered to be only partially blocked. Compared to the completely blocked cases, the hydrograph of partially blocked rivers only involves three stages (Fig. 6b and c). The first stage of the test case A-3, as in the completely blocked case, involves the deflection of landslide by the river which causes fluctuations in the river water level (Fig. 6d, $t^*=73.58$). In the second stage, the water level rises, albeit slowly because the river is not entirely obstructed and still allows continuous outward flow (Fig. 6e). Moreover, the potential energy of the water flow is lower than the complete blockage, leading to reduced erosion and breach expansion rates. Consequently, the time required to reach the peak water level is longer, and there are no distinct stages of water storage and breaching (Fig. 6f and g). The third stage is

similar to the B-3 test, where the water depth stabilizes, and the deposition of the rest landslide dam is unchanged (Fig. 6h, $t^* = 1635.19$).

The depth and velocity of the water flow influences the formation process of the landslide dam (Liao et al., 2019). Fig. 7 shows the deflection and the deposition of landslide moving into the flowing water as viewed from the top (Camera#3) and from the side (Camera#1). Outlines of the landslide deposits are drawn to further aid visibility. Fig. $7a_1$ - b_2 show the effect of the relative velocity between the river and the landslide on the trajectory and extent of landslide deflection. For a constant Fr_w (constant Q), the deflection decreases when the Fr_s is increased. On the other hand, increasing Fr_w while keeping a constant Fr_s (Fig. $7b_1$ - b_2) increases the deflection. The longitudinal profiles of experiments (A-3 and C-3) where the Fr_s is increased and Fr_w is held constant, likewise show that an increase in Fr_s leads to a higher minimum dam height. The preceding content demonstrates that the process of landslide dam formation is influenced by the landslide mobility and river flow regime. We quantify the relative mobility as:

$$Fr^* = Fr_s/Fr_w \tag{3}$$

When $Fr^* > 1$, the mobility of landslide dictates the deposit morphology, while the river flow is more important when $Fr^* < 1$.

The degree of deflection of the landslide mass can be quantified by a deflection factor which is the ratio of the farthest distance of the deposit upstream of the centerline (y = -10) L_1 and the farthest distance downstream of the centerline L_2 :

$$L^* = \frac{L_2}{L_1} \tag{4}$$

These lengths are measured from the profiles drawn from the snapshots (Fig. 7a₁-b₂). Since landslides tend to move along the direction of water flow, $L_2 > L_1$ and $L^* \ge 1$. Fig. 8a illustrates a negative correlation between L^* and Fr^* . As Fr^* is increased, the landslide momentum dominates, the influence of the river flow is minimal, and L^* approaches 1. This degree of deflection can be explained by the velocity and the time it takes for particles to move in the river. For small Fr^* , the velocity of the river significantly influences the landslide's movement along the flow

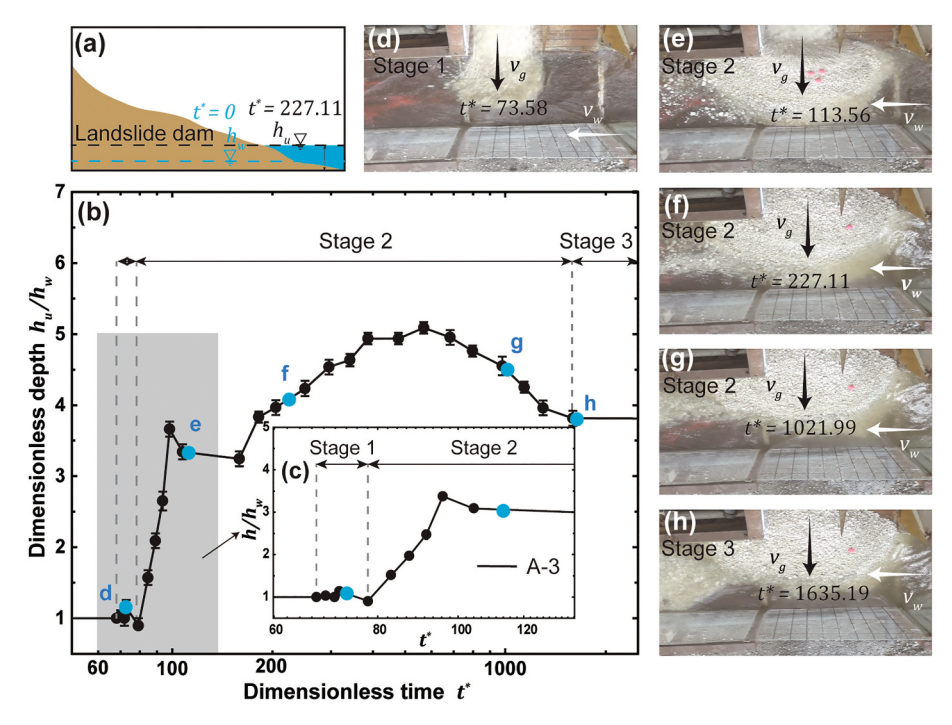


Fig. 6. The upstream water level change of the river with time of an example case A-3. (a) The schematic diagram of the water level change. (b) The evolution of the upstream dimensionless dammed water depth of sample case A-3 in dimensionless time t^* . (c) A closer look at the hydrograph in Stages 1–2. (d-h) Snapshots of the different stages of took by Camera#3.

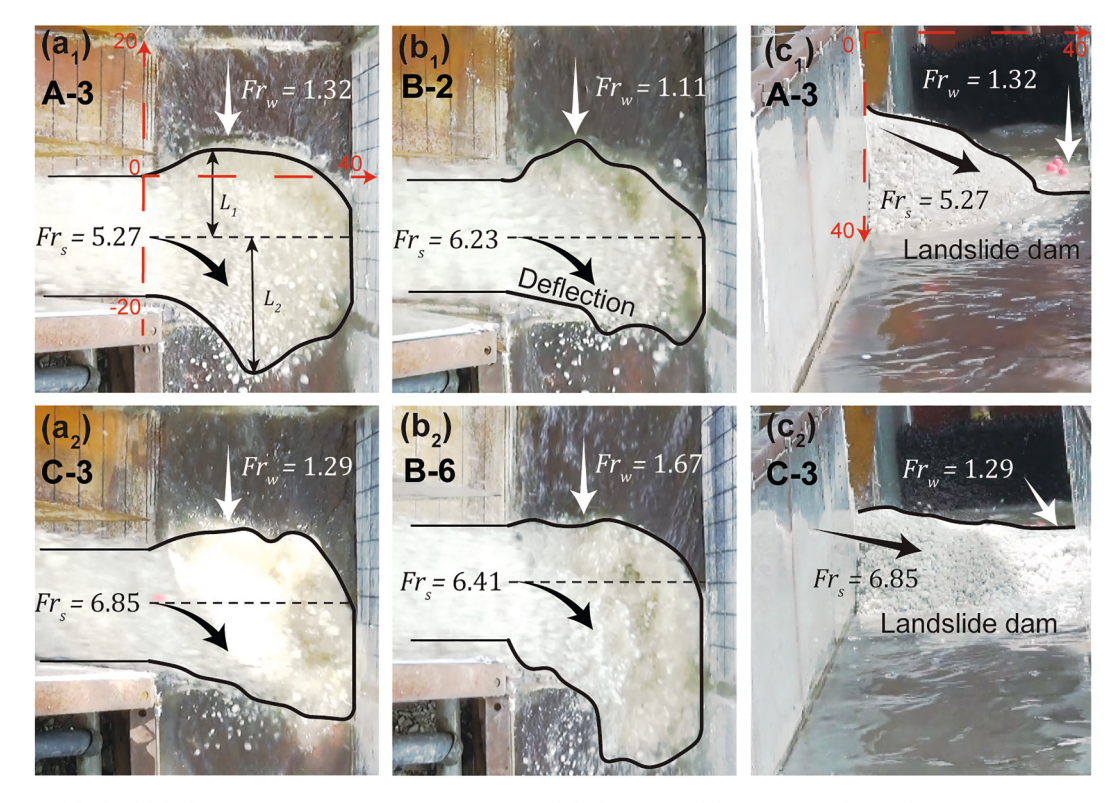


Fig. 7. The top view of the landslide deposition process for varying (a_1-a_2) Fr_s and (b_1-b_2) Fr_w , and their corresponding outlines (in cm). (c_1-c_2) Snapshots of the side view of the landslide deposits for different Fr_s and their corresponding deposit outlines.

direction, with increased velocities of river leading to greater particle transport distances and consequently a larger L^* . Conversely, when Fr^* is large, the landslide trajectory is only slightly altered by the low river flow. The minimal transport of particles along the direction of river flow results in a low L^* .

When the landslide is at rest, the particles that are not transported by the water flow stop into the channel and block the river. The minimum landslide dam height (h_d) is a key parameter which dictates the minimum water head and potential energy needed to overtop the dam. It is the vertical distance from the dam base to its lowest crest point and is obtained from Camera#1. Since the bottom of the dam is underwater, h_d is obtained as the distance of the top of the sidewall (0.4m) to the lowest point of the dam subtracted from the sidewall height. For instances where the minimum dam height is underwater and is near the sidewall, as is the case for all of our partially-blocked tests, it is estimated from the sidewalls viewed using Camera#2 (Fig. 7). Complete and partial blockage can therefore be divided according to the ratio of h_d and the depth of the river h_w :

$$H^* = \frac{h_d}{h_{\cdots}} \tag{5}$$

Fig. 8b shows that relative height H^* generally increases with Fr^* . When the Fr^* is small, the landslide mass mainly deposit in the junction of Channel No. 1 and Channel No. 2 (see Fig. 7c₁). Increasing Fr^* increases H^* (see Fig. 7c₁-c₂) and the landslide mass would quickly reach the opposite side of the junction. This is similar to the process of an actual high-speed landslide rushing to the opposite valley slope and climbing on it (Xu et al., 2013). Fig. 8b is split into two sections at $H^* = 1$: when $H^* \geq 1$ the river is completely blocked while it is partially blocked when $H^* < 1$.

3.2. Predicting degree of river blockage from Fr_s and Fr_w

We make use of the classification between completely blocked and

partially blocked states to formulate a relationship that may be used to predict river blockage based on the landslide mobility and river flow dynamics. Fig. 10 plots the Fr_w against the Fr_s for each test, with data points shaded according to the state of blockage determined from H^* (Fig. 8b). There is a clear separation between completely blocked and partially blocked cases. We use the single-layer perceptron algorithm to calculate the criteria for different degrees of river blockage:

$$Fr_s - A_0 Fr_w - A_1 = 0 (6)$$

where $A_0 = 2.91$ and $A_1 = 1.53$ are fitting parameters. Although, arbitrarily drawing a linear function to separate the degrees of blockage may also be effective given the clear separation of the data points, we choose to rely on a more data driven approach. This machine-learning based method allows for future adjustment of Eq. (6) and increases the classification accuracy by increasing the amount of input data (Shynk, 1990). The coefficients A_0 and A_1 may still change with additional data. Fig. 10 shows that, above the critical line, Fr_s is significantly larger than Fr_w resulting in river blockage; a greater distance from the critical line indicates a greater value of Fr^* and a smaller L^* . The opposite is true for data points below the critical line. When Fr_s remains constant, Fr_w determines the degree of river blockage and the formation of the landslide dam. As Fr_w increases, the velocity of the landslide mass needed to block the river likewise increases. In the experiments, Eq. (6) suggests that when $Fr_w = 0$, landslide mass still needs $Fr_s \ge 1.53$ to block the river channel, as the water will prevent the landslide from reaching the

In order to verify the reliability of the prediction model, we plot Fr_s against Fr_w for natural landslide dam cases in which the rivers are completely blocked (see Fig. 10). Dynamic parameters of these field cases are collected from the literature and are summarized in Table 2. Field surveys, remote sensing, and hydrological stations provided data on the river width, water flow depth, and the average flow at the time of the Yigong landslide blockage event (Yin, 2000; Li et al., 2020b). Numerical simulation and remote sensing data from Dai et al. (2019) and

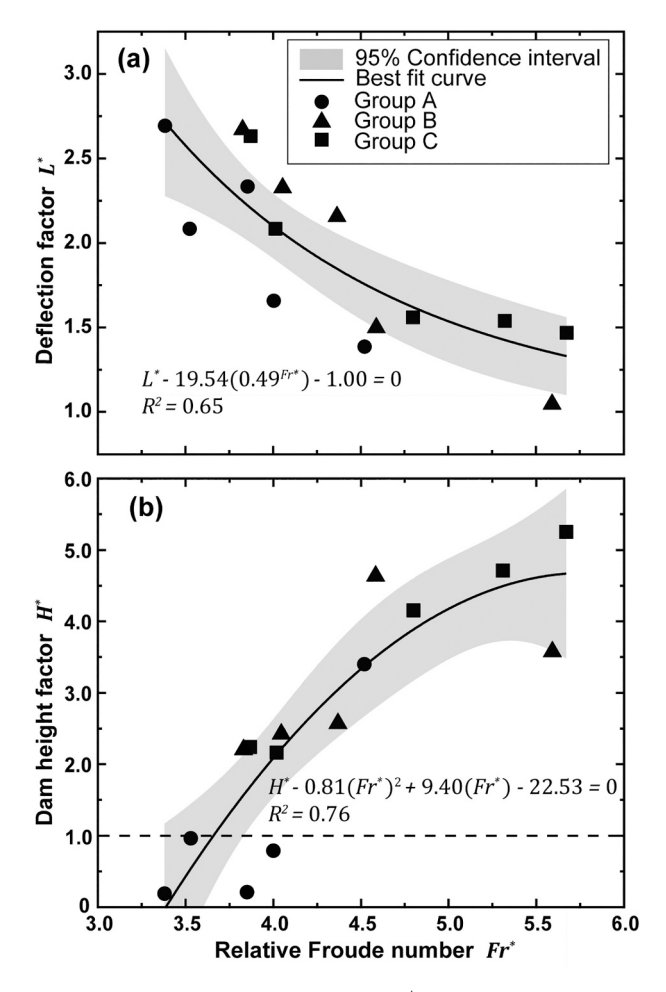


Fig. 8. The change of (a) the deflection factor L^* and (b) the dam height factor H^* with the relative Froude number Fr^* . The dashed line determines whether the river is completely ($H^* \geq 1$) or only partially blocked ($H^* < 1$).

Hao et al. (2021) allow for the calculation of the landslide velocity, flow depth, and slope angle. Wang et al. (2019) used combined drilling exploration results and numerical simulation analysis to investigate the development characteristics and river blockage mechanism of a landslide in the upper Jinsha River, which yielded the dynamic parameters needed for the calculation of Fr_s and Fr_w . Flow velocities and depth needed to estimate the Froude number of the Tangjiashan landslide is obtained from the detailed geological surveys of Hu et al. (2009) combined with pre-earthquake data. We note however a relatively large margin of error for the estimation of the flow depth since it was only estimated from depositional profiles. The information on the flow rate of

the Jinsha River and the terrain parameters of the Baige landslide were gathered through field surveys and dynamic deduction methods (Wu et al., 2022b; Zhou et al., 2022c; Tang and Jiang, 2023). Yang (2023) determined the dynamic parameters of the landslide by analyzing its characteristics observed after instability. The velocity derived from field investigation data is deemed more reliable. On the other hand, the velocity of the water flow can be calculated by dividing the average monthly discharge at the time of the event by the cross-sectional area of the river or by using propeller velocimeters and Acoustic Doppler Current Profilers (ADCP). Additionally, image-based methods such as Large-Scale Particle Image Velocimetry (LSPIV) are frequently employed to estimate river surface velocity (Wu et al., 2023). The limited availability of field measurements during landslide dam formation means that data estimated by the aforementioned methods, whether directly or indirectly, may contain errors compared to actual values, potentially impacting the final calculation of the Froude number.

Although the Froude numbers of these selected cases also fall within the range documented for other landslides and rivers in the literature. they are much smaller compared to those obtained from the experiments. To further support the use of real cases as validation for the classification model, we establish their geometric similarity with the experimental dams through the dimensionless numbers proposed by Peng and Zhang (2011) which has been used as design guidelines for landslide dam experiments (Shi et al., 2022; Li et al., 2024; Ma et al., 2024; Yang et al., 2024). These dimensionless numbers are the heightto-width ratio (H_d/W_d) , the lake shape coefficient $(V_l^{1/3}/H_d)$ and the dam shape coefficient $(V_d^{1/3}/H_d)$, wherein H_d is dam height, V_d is the part of landslide volume which blocks the river, V_l is the volume of water impounded by the landslide dam, W_d is width of landslide dam. In Fig. 9, we show that both our experiments and selected field cases collapse onto scaling curves along with numerous other landslide dams obtained from the literature (Hao et al., 2021; Shafieiganjeh et al., 2022; Wu et al., 2021, 2022a; Xu et al., 2013; Yang, 2023; Zhou et al., 2022b). This shows that the dynamics and interactions that control the landslide dam formation in these selected cases are similar to those in the experiments and the classification criteria is applicable to both scenarios.

All data points for the natural cases, in which the rivers were completely blocked, all fall above the critical line illustrating the effectiveness of the Froude number-based criterion in classifying the degree of blockage. By utilizing Eq. 6 and obtaining the Froude numbers of the landslide and the river, it is possible to predict whether landslides can completely or only partially block rivers.

3.3. The impact of blockage type and burst flood flow regimes on lateral erosion rates

The lateral erosion process $e_w = \frac{dw_w}{dt}$, results in the expansion of the dam breach with time t (Fig. 4b) and accelerates the dam failure process. Fig. 11 illustrates the variation of e_w over time for a partially (A-5) and

 Table 2

 Parameters of natural landslide dams (rivers).

Landslide dam				Slope	Froude number		Reference			
	Velocity (m/s)		Depth (m)		angle (°)					
	Landslide	River	Landslide	River		Landslide	River			
Yigong landslide (YL)	40.00	2.30	30.00	7.00	17.00	2.39	0.28	Yin (2000); Dai et al. (2019); Li et al. (2020b); Hao et al. (2021)		
Jinsha river blocked (JRB)	50.60	0.31	80.00	95.00	35.00	1.99	0.01	Wang et al. (2019)		
Tangjiashan landslide (TL)	30.00	0.19	46.10	4.00	50.00	1.76	0.03	Hu et al. (2009)		
Baige Landslide (BL)	64.20	0.72	45.00	12.00	50.50	3.83	0.07	Wu et al. (2022b); Zhou et al. (2022c); Tang and Jiang (2023); Yang (2023)		

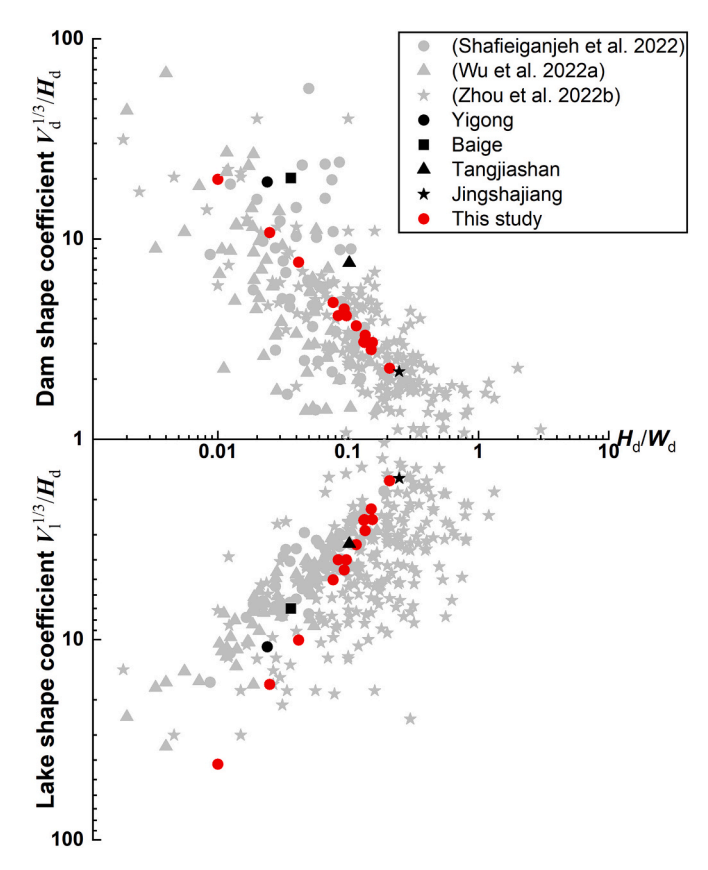


Fig. 9. Ternary plot of dimensionless parameters that characterize the geometries of the experimental landslide dams (red circles) and the cases used for model validation (black symbols). Other landslide dams (gray symbols), not used for validation, are also included to show the generality of the geometrical scaling (Shafieiganjeh et al., 2022; Wu et al., 2022a; Zhou et al., 2022b).

completely (B-6) blocked river. These cases have similar Fr^* but different degrees of river blockage (show in Table 1). Despite similarities in the general trend in both conditions, differences emerge at the beginning of erosion. Specifically, the erosion rate commences at zero and ascends in completely blocked rivers before decreasing to a constant value over a long period of time. In the partially blocked conditions, erosion rates initiate from a non-zero value, rises up to a maximum value, and decays toward a near zero erosion rate. Furthermore, the maximum erosion rate in the completely blocked scenario surpasses that of the partially blocked case due to the higher potential energy of the burst flood.

The erosion rate of the landslide dam is directly influenced by the shear stress exerted by the water flow and the resistance of sediment against erosion resistance. When the shear stress of the water flow exceeds the erosion resistance, particles from the landslide dam can be entrained into the water flow. Based on mechanical equilibrium principles, Partheniades (1965) proposed a linear erosion equation that quantifies the erosion rate, which has been widely applied in landslide dam studies (Chang and Zhang, 2010; Shi et al., 2022; Chen et al., 2023). This equation has been further validated by large-scale experiments (Zhou et al., 2019a; Zhou et al., 2022b), and is expressed as follows:

$$e_w = k_{dw}(\tau_w - \tau_{cw}) \tag{7}$$

where k_{dw} ($cm^3/N-s$) is a dimensional constant of erodibility and depends on the dam material properties (Garcia-Castellanos and O'Connor, 2018); τ_w (Pa) is the shear stress exerted by the water flow on the landslide dam; τ_{cw} (Pa) is the apparent erosion resistances (also called critical shear stress) which is influenced by the cohesive nature of the material. Different equations have been proposed in the literature to calculate k_{dw} and τ_{cw} , some of them are summarized in Table 3. Hanson

Table 3 Equations to calculate the k_{dw} and $au_{cw.}$

Equation		References
$k_{dw1} = 0.2\tau_{cw}^{-0.5}$	(8)	Hanson and Simon (2001)
$k_{dw2} = 0.43\tau_{cw}^{-0.79}$	(9)	Al-Madhhachi et al. (2013)
$ au_{cw1} = 3.54 ig(10^{-28.10 d_{50}} ig)$	(10)	Smerdon and Beasley (1961)
$ au_{\mathrm{cw2}} = 0.015(ho_b - 1000)^{0.73}$	(11)	Mitchener and Torfs (1996)

and Simon (2001) proposed a relationship for k_{dw} and the critical shear stress τ_{cw} for cohesive materials (Eq. 8) based on in situ jet-testing measurements. Al-Madhhachi et al. (2013) on the other hand established a formula for k_{dw} and τ_{cw} for non-cohesive materials (Eq. 9). Smerdon and Beasley (1961) calculate τ_{cw} based on the median particle size (d_{50}) of landslide dam (Eq. 10) while Mitchener and Torfs (1996), based on the large number of laboratory and field tests, found that density change can impact the critical shear stress, and derived a relationship between τ_{cw} and bulk density of the dam ρ_b (Eq. 11).

The lateral shear stresses τ_w can be calculated from Manning's equation:

$$\tau_w = \varepsilon \frac{\rho g n^2 v_b^2}{h_b^{1/3}} \tag{12}$$

where $\rho\left(kg/m^3\right)$, $v_b\left(m/s\right)$, and $h_b\left(m\right)$ are the density, velocity, and depth of the eroding water flow respectively. The Manning's coefficient n is related to the median particle size $d_{50}\left(m\right)$, through $n=d_{50}^{1/6}/A_n$ where $A_n=20$ is an empirical coefficient. The value of A_n used here is based on Wu (2013) for fixed streambeds. The lateral shear stresses can be related to the basal shear stress through formulas proposed by Yang and Lim (1997) and Yang and Lim (1998):

$$\varepsilon = \begin{cases} \frac{\left(1 - 0.25 \frac{W}{h_b}\right) \left(1 + \frac{P_b}{P_w}\right)}{1 - \left(1 - 0.25 \frac{W}{h_b}\right) \left(1 + \frac{P_w}{P_b}\right)} \frac{W}{h_b} \le 2\\ \frac{\frac{h_b}{W} \left(1 + \frac{P_b}{P_w}\right)}{1 - \frac{h_b}{W} \left(1 + \frac{P_w}{P_b}\right)} \frac{W}{h_b} \ge 2 \end{cases}$$
(13)

where P_b is the wetted perimeter of the river bed, which is equivalent to the breach channel; P_w is the wetted perimeter of the channel sidewall, which is equal to the depth of water flow; and W is the width of the flume. Substituting Eq. 12 into 7 gives:

$$\mathbf{e}_{w} = k_{dw} \left(\varepsilon \frac{\rho g n^{2} v_{b}^{2}}{h_{b}^{1/3}} - \tau_{cw} \right) \tag{14}$$

Exploring the relationship between lateral erosion rates and water flow regimes facilitates the prediction of erosion intensity under varying flow conditions, thereby providing a foundation for effective erosion control measures. Therefore, the dependence of the lateral shear stress on the outburst flow velocity and height can be summarized into an outburst flood Froude number Fr_b . Eq. 14 can therefore be re-written as:

$$e_{w} = k_{dw} \left(\varepsilon \rho n^{2} F r_{b}^{2} g^{2} h_{b}^{2/3} - \tau_{cw} \right) \tag{15}$$

Eqs. 8–11 show that k_{dw} and τ_{cw} are only related to the landslide material, while ρ , g and n in Eq. 12 are constant for all experiments. Therefore, only ε , $h_b^{2/3}$ and Fr_b are the quantities that vary with the dynamics of the eroding water flow in Eq. 15. To obtain a direct relationship between e_w and Fr_b we first relate Fr_b with $\varepsilon h_b^{2/3}$. Fig. 12 shows

the negative dependence of $\varepsilon h_b^{2/3}$ with Fr_b for all test cases (except for some test whose erosion process could not be clearly captured by Camera#2) which can be defined by the function:

$$\varepsilon h_b^{2/3} - 0.11 \left(e^{-\frac{Fr_b}{0.98}} \right) - 0.04 = 0$$
 (16)

The scatter of the data points is due to the measurement errors that result from the surging of breaching flows. Substituting Eq. 16 into Eq. 15 results in an equation which primarily depends on Fr_b :

$$e_{w} = k_{dw} \left\{ \left[0.11 \left(e^{-\frac{Fr_{b}}{0.98}} \right) + 0.04 \right] Fr_{b}^{2} \rho g^{2} n^{2} - \tau_{cw} \right\}$$
(17)

resulting in an equation which primarily depends on Fr_b . The first term in Eq. 17 is simply the flow shear stress expressed in terms of Fr_b and will be denoted as τ_{Fr} .

We plot in Fig. 13 the relationship of Fr_b with e_w for dams that completely (test A-3, circle) and partially (test B-4, triangle) block rivers. There is no noticeable difference in the change of the erosion rates with the outburst flood of completely blocked (empty circles) and partially blocked dams (shaded triangles). The lateral erosion rate increases with the increase of Fr_b . The e_w of the partially blocked case is primarily distributed under the completely blocked cases. The solid lines are predictions made with Eq. 17 calculated using different k_{dw} (Eqs. 8 and 9) and τ_{cw} (Eqs. 10 and 11). Best-fits using k_{dw2} show closer correspondence to the experimental data despite the fact that Eq. 9 is derived from experiments conducted on non-cohesive material. The considerable deviation of the data points primarily stem from the erosion rate equation being derived from an idealized and widely used empirical equation, which may not be perfectly suitable for this experiment due to differences in material properties. Additionally, the water volume in the Part B of Fig. 4c is simplified by approximating it as a trapezoidal prism. However, this method of simplifying the geometry of the dammed lake introduces a series of errors, as the calculated volume may not accurately represent the true volume. In contrast, Eq. 8, derived from cohesive material, is fundamentally different from the conditions in this study, rendering this fitting curve unsuitable for the data in this study.

4. Discussion

We conduct flume tests to investigate the dependence of the land-slide dam deposit morphology, quantified by the deflection and height factors, and degree of river blockage on both the landslide mobility and river hydrodynamics. Results yield a criterion for classifying complete and partial river blockage which may be used for the prediction of the degree of landslide damming. The criterion is based on the Froude number of the landslide and the river flow. Despite limitations arising from the unavoidable simplifications and scale of the experimental setup, this research can contribute to the prediction of river blockage under different regimes of landsliding and river flows.

As demonstrated in Fig. 10, the possible Froude number when a landslide occurs is estimated through field surveys, and the Froude number of the river can be obtained from the hydrological stations. These data provide estimates of the Froude numbers that can be expected from events having similar scale and geological setting, which can then be substituted into Eq. (6) through which the possibility of complete or partial river blockage can be evaluated. More data is required to refine the parameters in Eq. 6 (such as A_0 and A_1) to enhance its applicability but the results so far obtained are promising. According to the phase diagram in Fig. 10, a critical Froude number Fr_g of 1.53 is required to block the channel, even when the water flow velocity is negligible, as the presence of water dissipates the momentum of the landslide. The important parameters not addressed in this work are the width and depth of the river. A wider river allows for a longer run-out

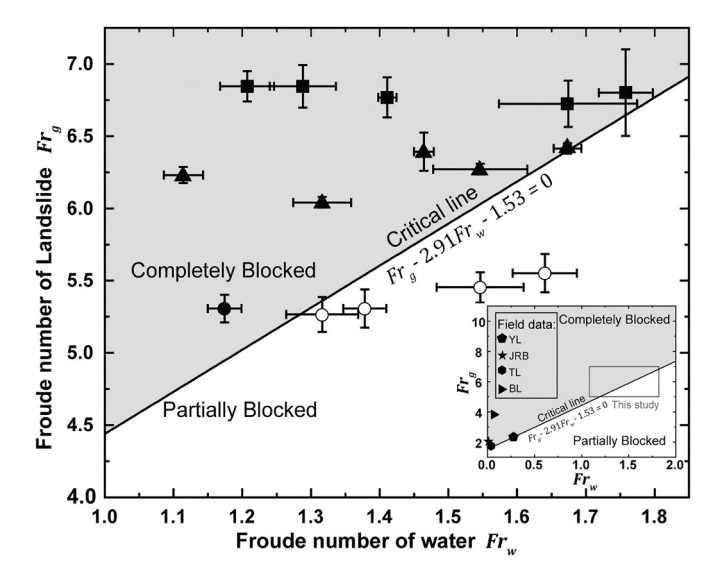


Fig. 10. Experimental cases are plotted by Fr_s and Fr_w , with black and white points showing complete and partial blockages. Different shapes represent experimental groups (see Table 1). The critical line is from Eq. 6, with gray and white regions for complete and partial blockages. The inset shows natural events: Yigong (YL), Jinsha (JRB), Tangjiashan (TL), and Baige (BL) landslides.

distance for the landslide, exposing it to greater hydrodynamic forces. Consequently, a slow or less massive landslide may be unable to block a wide river, even though it could effectively block a narrower one. Additionally, a deeper river requires more landslide material to fill its volume and facilitates greater fluid interaction, which dampens the motion of the landslide. Previous studies have highlighted the significance of river width and depth as key topographic factors influencing the likelihood of a landslide blocking a river. Several studies have proposed equations predicting landslide-induced blockages based on river width (Chen and Chang, 2015; Chen et al., 2021a; Yu et al., 2022). In addition, this experiment used only dry and non-cohesive materials to investigate river blockage by the landslide. However, recent studies have shown that material of landslide play a crucial role in determining the formation of landslide dams, characteristics of dam structural, and the processes of breach erosion (Zhou et al., 2022d; Zhang et al., 2023). While these factors were not considered in this study, the effects of channel dimensions and landslide material will be investigated in future research. Moreover, the criterion appears to be more appropriate for cases where high-mobility landslides block rivers, due to a lack of experimental studies addressing slow-moving landslides in here. Furthermore, this study does not consider the stability and longevity of the dam, and peak discharge of the burst flood.

5. Conclusions

Through flume model tests, we simulate the processes of dam formation and breaching while change both the landslide mobility and the river flow dynamics. Based on our experiments, we conclude that:

(1) The landslide mobility and the river flow, quantified by their relative Froude numbers $Fr^* = Fr_s/Fr_w$, determine the formation process and shape of landslide dam. Landslide entering rivers are deflected along the direction of the river flow. When Fr^* is large, landslide inertia significantly overpowers the river flow resulting in minimal deflection. After the landslide deposits on the river valley, degree of blockage is assessed based on the relative height of the dam and the river water level. Increasing Fr^* likewise increases the degree of blockage.

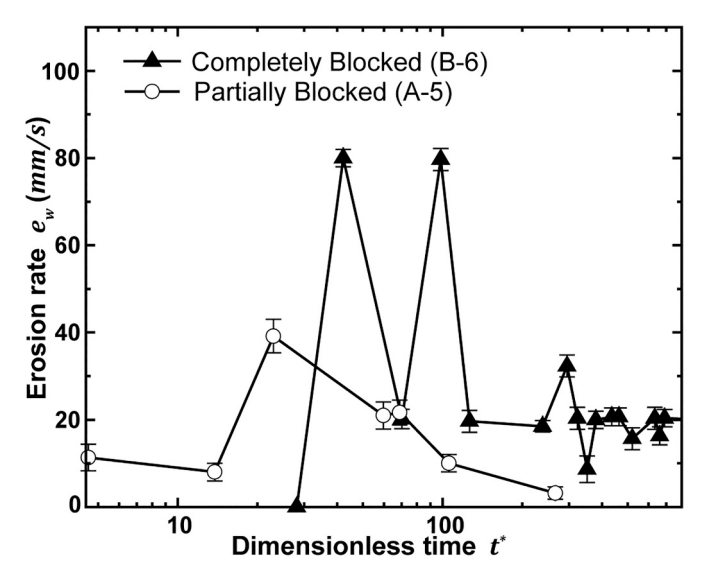


Fig. 11. The dimensionless temporal (t^*) evolution of the erosion rate e_w for completely (B-6) and partially blocked rivers (A-5).

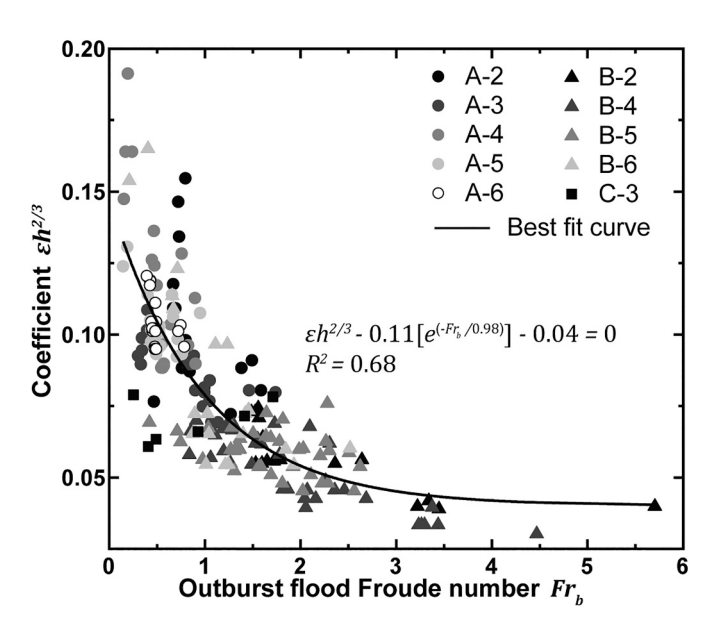


Fig. 12. The relationship between the Froude number of outburst flood Fr_b and the coefficient $\varepsilon h_b^{2/3}$ for all test cases (except for some test whose erosion process could not be clearly captured by Camera#2).

- (2) The complete or partial blockage of rivers by landslides can also be determined from Fr^* . We draw a threshold in the $Fr_s Fr_w$ parameter space that classifies completely blocked and partially blocked rivers. The derived threshold is able to determine the degree of river blockage.
- (3) Experimental data reveal a positive correlation between the lateral erosion rate of the dam and the Froude number of burst floods (Fr_b) . The lateral erosion rate increases with the Froude number of the burst flood. We derive a formula that reflects the relationship of the burst flood and erosion rates of the landslide dam. This result enhances the understanding of the burst flood dynamics in case of dam breaching.

Notations

 A_0, A_1, A_n Fitting parameters; Fitting parameters; Empirical coefficient

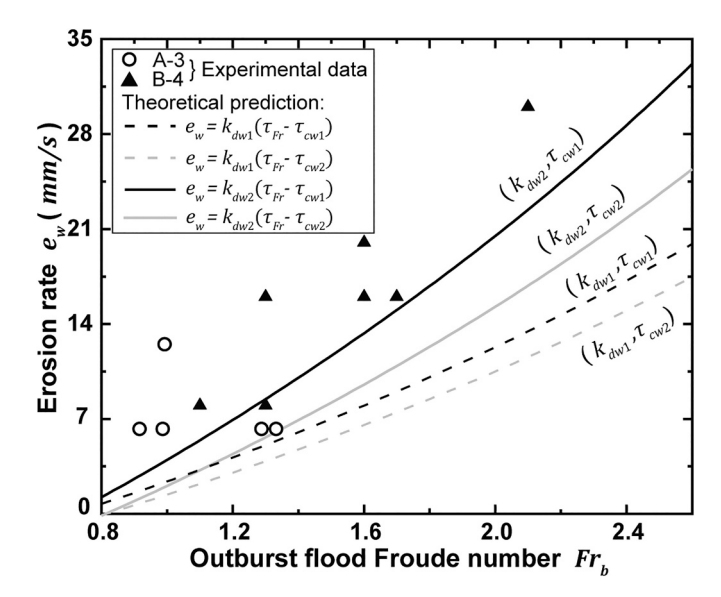


Fig. 13. The relationship of the e_w with Fr_b . The circles and triangles are measured data from tests A-3 (partially blocked) and B-4 (completely blocked), respectively. These curves are predictions obtained from Eq. 17 calculated using the different expression for k_{dw} and τ_{cw} .

to calculate Manning's coefficient

 d_{50} Median particle size

 e_w Lateral erosion rate

 $Fr, Fr_s, Fr_w, Fr_b, Fr^*$ Froude number; Froude number of landslide; Froude number of water flow; Froude number of outburst flood; and relative Froude number

Acceleration due to gravity

 h_d, h_s, h_w Minimum height of landslide dam (vertical distance from the dam bottom to the lowest point on the landslide dam); flow depth of landslide; and initial depth of water flow

 $h, h_u, \Delta h_r, h_b, H^*, H_d$ Flow depth of the fluid; depth of upstream water flow; depth-change of the dammed lake; depth of the burst water: relative height; and dam height

 k_{dw}, k_{dw1}, k_{dw2} Dimensional constants of erodibility; erodibility calculate by Eq. 8; and erodibility calculate by Eq. 9

 L, L_1, L_2, L^* Slide distance of landslide; the longest distance of the deposit upstream of the centerline; and the longest distance downstream of the centerline; deflection factor

Manning's coefficient

 P_b, P_w Wetted perimeter of the bed; and wetted perimeter of the channel sidewall

 Q, Q_b Inflow rate; and breach discharge

 $t, t^*, t_i, \Delta t$ The initial time of the experiments; dimensionless time; the time at step i; and fixed time interval

 v, v_s, v_w, v_b Velocity of the fluid; velocity of landslide; velocity of water flow; and velocity of burst water

 $\Delta V_b, V_d, \ V_l$ Burst volume of the breach flood in fixed time; the part of landslide volume which blocks the rive; and the volume of water ponded behind the landslide dam

 $w_w, w_{wi}, \Delta w, W, W_d$ The width of dam breach; the width at step i; width-change of the dam breach on fix time, width of the flume; width of landslide dam

 α Interface friction angle

slope angle

 ρ, ρ_b Density of burst water; bulk density of the material

 $au_w, au_{cw}, au_{cw1}, au_{cw2}$ Shear stress exerted by the water flow on the landslide dam; signifies apparent erosion resistances; erosion resistances calculated by Eq. 10; and signifies apparent erosion resistances calculate by Eq. 11

The coefficient relates the lateral with the basal shear stress

Flow shear rate expressed in terms of Fr_h

CRediT authorship contribution statement

Hongwei Luo: Writing – review & editing, Writing – original draft, Methodology. Gordon G.D. Zhou: Writing – review & editing, Supervision, Methodology, Funding acquisition. Xueqiang Lu: Writing – review & editing, Supervision, Methodology. Kahlil F.E. Cui: Writing – review & editing, Supervision, Methodology. Yuting Zhao: Writing – review & editing. Yunxu Xie: Writing – review & editing, Funding acquisition. Wei Zhong: Writing – review & editing. Jiawen Zhou: Writing – review & editing. Alessandro Pasuto: Writing – review & editing.

Declaration of competing interest

The authors declare that they have no known competing financial interests or personal relationships that could have appeared to influence the work reported in this paper.

Data availability

Data will be made available on request.

Acknowledgements

The authors acknowledge the financial support from the National Key R&D Program of China (No. 2023YFC3008300, 2023YFC3008302), National Natural Science Foundation of China (Grant 12250410257), the Science and Technology Research Program of Institute of Mountain Hazards and Environment, Chinese Academy of Sciences (No. IMHEZDRW-03), Key Collaborative Research Program of the Alliance of International Science Organizations (Grant ANSO-CR-KP-2021-07), Sichuan Science and Technology Program (2024NSFJQ0043), and State Key Laboratory of Hydraulics and Mountain River Engineering, Sichuan University (Grant No.SKHL2308).

References

- Al-Madhhachi, A.-S.T., Hanson, G.J., Fox, G.A., Tyagi, A.K., Bulut, R., 2013. Measuring soil erodibility using a laboratory "mini" JET. Trans. ASABE 56, 901–910. https:// doi.org/10.13031/trans.56.9742.
- Chang, D.S., Zhang, L.M., 2010. Simulation of the erosion process of landslide dams due to overtopping considering variations in soil erodibility along depth. Nat. Hazards Earth Syst. Sci. 10, 933–946. https://doi.org/10.5194/nhess-10-933-2010.
- Chen, C.-Y., Chang, J.-M., 2015. Landslide dam formation susceptibility analysis based on geomorphic features. Landslides 13, 1019–1033. https://doi.org/10.1007/ s10346_015_06715.
- Chen, S.-C., Lin, T.-W., Chen, C.-Y., 2015. Modeling of natural dam failure modes and downstream riverbed morphological changes with different dam materials in a flume test. Eng. Geol. 188, 148–158. https://doi.org/10.1016/j.enggeo.2015.01.016.
- Chen, K.-T., Chen, X.Q., Hu, G.S., Kuo, Y.S., Chen, H.Y., 2019. Effects of river flow velocity on the formation of landslide dams. J. Mt. Sci. 16, 2502–2518. https://doi. org/10.1007/s11629-018-5319-1.
- Chen, K.-T., Chen, T.-C., Chen, X.-Q., Chen, H.-Y., Zhao, W.-Y., 2021a. An experimental determination of the relationship between the minimum height of landslide dams and the run-out distance of landslides. Landslides 18, 2111–2124. https://doi.org/ 10.1007/s10346-020-01605-1.
- Chen, Z., Rickenmann, D., Zhang, Y., He, S., 2021b. Effects of obstacle's curvature on shock dynamics of gravity-driven granular flows impacting a circular cylinder. Eng. Geol. 293. https://doi.org/10.1016/j.enggeo.2021.106343.
- Chen, C., Wang, Y., Zhang, J., Zhang, H., Li, H., Chen, Q., 2023. A preliminary study of landslide dam failures induced by the combined influence of piping and overtopping. J. Hydrol. 625. https://doi.org/10.1016/j.jhydrol.2023.129984.
- Cheng, H., Zhang, B., Huang, Y., 2022. SPH-Based numerical study on the influence of baffle height and inclination on the interaction between granular flows and baffles. Water 14. https://doi.org/10.3390/w14193063.
- Choi, C.E., Ng, C.W.W., Au-Yeung, S.C.H., Goodwin, G.R., 2015. Froude characteristics of both dense granular and water flows in flume modelling. Landslides 12, 1197–1206. https://doi.org/10.1007/s10346-015-0628-8.
- Costa, J.E., Schuster, R.L., 1988. The formation and failure of natural dams. Geol. Soc. Am. Bull. 100, 1054–1068. https://doi.org/10.1130/0016-7606(1988)100<1054: TFAFON>2.3.CO;2.

- Coussot, P., Meunier, M., 1996. Recognition, classification and mechanical description of debris flows. Earth Sci. Rev. 40, 209–227. https://doi.org/10.1016/0012-8252(95)
- Cui, P., Zhu, Y.-Y., Han, Y.-S., Chen, X.-Q., Zhuang, J.-Q., 2009. The 12 May Wenchuan earthquake-induced landslide lakes: distribution and preliminary risk evaluation. Landslides 6, 209–223. https://doi.org/10.1007/s10346-009-0160-9.
- Cui, P., Zeng, C., Lei, Y., 2015. Experimental analysis on the impact force of viscous debris flow. Earth Surf. Process. Landf. 40, 1644–1655. https://doi.org/10.1002/ esp.3744.
- Dai, X., Yin, Y., Xing, A., 2019. Simulation and dynamic analysis of Yigong rockslide-debris avalanche-dam breaking disaster chain. Chin. J. Geol. Hazard Control 30, 1–8 (in Chinese). https://www.doc88.com/p-87516160819811.html.
- Dong, J.-J., Tung, Y.-H., Chen, C.-C., Liao, J.-J., Pan, Y.-W., 2011. Logistic regression model for predicting the failure probability of a landslide dam. Eng. Geol. 117, 52–61. https://doi.org/10.1016/j.enggeo.2010.10.004.
- Ermini, L., Casagli, N., 2003. Prediction of the behaviour of landslide dams using a geomorphological dimensionless index. Earth Surf. Process. Landf. 28, 31–47. https://doi.org/10.1002/esp.424.
- Fan, X., Tang, C.X., van Westen, C.J., Alkema, D., 2012. Simulating dam-breach flood scenarios of the Tangjiashan landslide dam induced by the Wenchuan Earthquake. Nat. Hazards Earth Syst. Sci. 12, 3031–3044. https://doi.org/10.5194/nhess-12-3031-2012.
- Fan, X., Scaringi, G., Korup, O., West, A.J., Westen, C.J., Tanyas, H., Hovius, N., Hales, T. C., Jibson, R.W., Allstadt, K.E., Zhang, L., Evans, S.G., Xu, C., Li, G., Pei, X., Xu, Q., Huang, R., 2019. Earthquake-induced chains of geologic hazards: patterns, mechanisms, and impacts. Rev. Geophys. 57, 421–503. https://doi.org/10.1029/2018RG000626.
- Fan, X., Dufresne, A., Siva Subramanian, S., Strom, A., Hermanns, R., Tacconi Stefanelli, C., Hewitt, K., Yunus, A.P., Dunning, S., Capra, L., Geertsema, M., Miller, B., Casagli, N., Jansen, J.D., Xu, Q., 2020. The formation and impact of landslide dams – State of the art. Earth Sci. Rev. 203. https://doi.org/10.1016/j. earscirev.2020.103116.
- Garcia-Castellanos, D., O'Connor, J.E., 2018. Outburst floods provide erodability estimates consistent with long-term landscape evolution. Sci. Rep. 8, 10573. https://www.ncbi.nlm.nih.gov/pubmed/30002507.
- Hanson, G.J., Simon, A., 2001. Erodibility of cohesive streambeds in the loess area of the midwestern USA. Hydrol. Process. 15, 23–38. https://doi.org/10.1002/hyp.149.
- Hao, Y., Changbao, G., Ruian, W., Yiqiu, Y., Zhihua, Y., 2021. Research progress and prospects of the giant Yigong long run-out landslide, Tibetan Plateau China. Geol. Bull. China 1–19 (in Chinese). https://kns.cnki.net/kcms/detail/11.4648.P.2021122 7.1821.004.html.
- Hu, X., Huang, R., Shi, Y., Lu, X., Zhu, H., Wang, X., 2009. Analysis of blocking river mechanism of Tangjiashan landslide and dam-breaking mode of its barrier dam. Chin. J. Rock Mech. Eng. 28, 181–189 (in Chinese).
- Hu, H., Zhou, G.G.D., Song, D., Cui, K.F.E., Huang, Y., Choi, C.E., Chen, H., 2020. Effect of slit size on the impact load against debris-flow mitigation dams. Eng. Geol. 274. https://doi.org/10.1016/j.enggeo.2020.105764.
- Jin, J., Chen, G., Meng, X., Zhang, Y., Shi, W., Li, Y., Yang, Y., Jiang, W., 2022. Prediction of river damming susceptibility by landslides based on a logistic regression model and InSAR techniques: a case study of the Bailong River Basin, China. Eng. Geol. 299. https://doi.org/10.1016/j.enggeo.2022.106562.
- Korup, O., 2002. Recent research on landslide dams a literature review with special attention to New Zealand. Prog. Phys. Geogr. Earth Environ. 26, 206–235. https:// doi.org/10.1191/0309133302pp333ra.
- Li, D., Nian, T., Wu, H., Wang, F., Zheng, L., 2020a. A predictive model for the geometry of landslide dams in V-shaped valleys. Bull. Eng. Geol. Environ. 79, 4595–4608. https://doi.org/10.1007/s10064-020-01828-5.
- Li, Z., Tang, T., Yuan, X., Yu, G., 2020b. Impacts of river-blocking barrier dams on morphological processes of upper alluvial channel in Yarlung Tsangpo Grand Canyon. J. Yangtze River Sci. Res. Inst. 37, 16–21 (in Chinese). http://kns.cnki.net/ kcms/detail/42.1171.TV.20191008.1057.028.html.
- Li, X., Chen, H., Chen, X., Wang, T., Jiang, Y., Ruan, H., 2024. Experimental study on the stability of noncohesive landslide dams based on seepage effect. Eng. Geol. 341, 107708. https://www.sciencedirect.com/science/article/pii/S0013795224003089.
- Liao, H.-M., Yang, X.-G., Lu, G.-D., Tao, J., Zhou, J.-W., 2019. Experimental study on the river blockage and landslide dam formation induced by rock slides. Eng. Geol. 261. https://doi.org/10.1016/j.enggeo.2019.105269.
- Luo, H.Y., Zhang, L.M., He, J., Yin, K.S., Wang, H.J., Zhou, G.G.D., Peng, M., Cheng, Q. G., 2022. Energy transfer mechanisms in flow-like landslide processes in deep valleys. Eng. Geol. 308. https://doi.org/10.1016/j.enggeo.2022.106798.
- Ma, C., Peng, M., Zhang, L., Shi, Z., Zhou, J., Chen, H., Zhu, Y., Li, Z., 2024. Erosion, deposition and breach evolution of landslide dams composed of various dam material types based on flume tests. Eng. Geol. 337, 107598. https://www.sciencedirect.com/science/article/pii/S0013795224001984.
- Mitchener, H., Torfs, H., 1996. Erosion of mud/sand mixtures. Coast. Eng. 29, 1–25. https://doi.org/10.1016/S0378-3839(96)00002-6.
- Nian, T.-K., Wu, H., Li, D.-Y., Zhao, W., Takara, K., Zheng, D.-F., 2020. Experimental investigation on the formation process of landslide dams and a criterion of river blockage. Landslides 17, 2547–2562. https://doi.org/10.1007/s10346-020-01494-4.
- Nian, T.-K., Wu, H., Takara, K., Li, D.-Y., Zhang, Y.-J., 2021. Numerical investigation on the evolution of landslide-induced river blocking using coupled DEM-CFD. Comput. Geotech. 134. https://doi.org/10.1016/j.compgeo.2021.104101.
- Niu, Z., Meng, C., Xu, W., Di, B., Long, Y., Yang, H., 2023. Experimental study on whole process of river blockage and dam break under different hydrodynamic conditions. Front. Earth Sci. 10. https://doi.org/10.3389/feart.2022.977246.

- Partheniades, E., 1965. Erosion and deposition of cohesive soils. J. Hydraul. Div. 91, 105–139. https://doi.org/10.1061/JYCEAJ.0001165.
- Peng, M., Zhang, L.M., 2011. Breaching parameters of landslide dams. Landslides 9, 13–31. https://doi.org/10.1007/s10346-011-0271-y.
- Schuster, R.L., 1986. Landslide Dams: Processes, Risk, and Mitigation. https://cedb.asce.org/CEDBsearch/record.jsp?dockey=0048507.
- Seip, K.L., 2004. The Froude number stick, an evaluation. River Res. Appl. 20, 99–102. https://doi.org/10.1002/rra.717.
- Shafieiganjeh, R., Ostermann, M., Schneider-Muntau, B., Gems, B., 2022. Assessment of the landslide dams in Western Austria, Bavaria and Northern Italy (part of the Eastern Alps): data inventory development and application of geomorphic indices. Geomorphology 415. https://doi.org/10.1016/j.geomorph.2022.108403.
- Shi, Z., Zhang, G., Peng, M., Zhang, Q., Zhou, Y., Zhou, M., 2022. Experimental investigation on the breaching process of landslide dams with differing materials under different inflow conditions. Materials (Basel) 15. https://www.ncbi.nlm.nih. gov/pubmed/35329478.
- Shi, N., Li, Y., Wen, L., Zhang, Y., Zhang, H., 2023. Longevity prediction and influencing factor analysis of landslide dams. Eng. Geol. 327, 107334. https://www.sciencedirec t.com/science/article/pii/S0013795223003526.
- Shynk, J.J., 1990. Performance surfaces of a single-layer perceptron. IEEE Trans. Neural Netw. 1, 268–274. https://ieeexplore.ieee.org/document/80252.
- Smerdon, E.T., Beasley, R.P., 1961. Critical tractive forces in cohesive soils. Agric. Eng. 42, 26–29. http://refhub.elsevier.com/S0341-8162(20)30451-3/h0265.
- Swanson, F.J., Oyagi, N., Tominaga, M., 1986. Landslide dams in Japan. In: Landslide Dams: Processes, Risk, and Mitigation. ASCE, pp. 131–145. https://api.semanticsch olar.org/CorpusID:128854543.
- Tacconi Stefanelli, C., Segoni, S., Casagli, N., Catani, F., 2016. Geomorphic indexing of landslide dams evolution. Eng. Geol. 208, 1–10. https://doi.org/10.1016/j. engge0.2016.04.024
- Takayama, S., Imaizumi, F., 2022. Effects of coarse particles on downstream face erosion processes and outflow discharge during the overtopping of a landslide dam. Landslides 20, 351–366. https://doi.org/10.1007/s10346-022-01973-w.
- Tang, Y., Jiang, Q., 2023. Study on application of SPH-DEM fluid-structure interaction to simulating Baige Landslide in Jinsha River. J. Changjiang Inst. Technol. 40, 1–8 (in Chinese).
- Wang, J., Ren, G., Ge, H., 2019. Development Characteristics and River-blocking Mechanism of a Mega-landslide in the Upper Reach of Jinsha River. J. Yangtze River Sci. Res. Inst. 36, 46-51, 57. (in Chinese). http://kns.cnki.net/kcms/detail/42.1171. TV.20180113.1332.006.html.
- Wu, W., 2013. Simplified physically based model of earthen embankment breaching. J. Hydraul. Eng. 139, 837–851. https://doi.org/10.1061/(ASCEHY.1943-7900.0000741.
- Wu, H., Nian, T.-K., Chen, G.-Q., Zhao, W., Li, D.-Y., 2020. Laboratory-scale investigation of the 3-D geometry of landslide dams in a U-shaped valley. Eng. Geol. 265. https:// doi.org/10.1016/j.enggeo.2019.105428.
- Wu, R.A., Ma, H., Zhang, J., Yang, Z., Li, X., Ni, J., Zhong, N., 2021. Developmental characteristics and damming river risk of the Woda landslide in the upper reaches of the Jinshajiang River. Hydrogeol. Eng. Geol. 48, 120–128. https://doi.org/ 10.16030/j.cnki.issn.1000-3665.202104036.
- Wu, H., Trigg, M.A., Murphy, W., Fuentes, R., 2022a. A new global landslide dam database (RAGLAD) and analysis utilizing auxiliary global fluvial datasets. Landslides 19, 555–572. https://doi.org/10.1007/s10346-021-01817-z.
- Wu, X., Cao, S., Zhang, L., 2022b. Mechanism and development trends of the Baige Landslide on the Jinsha River. Acta Geol. Sichuan 42. https://www.zhangqiaokeyan. com/academic-journal-cn_acta-geologica-sichuan_thesis/02012100040619.html.
- Wu, Y., Zhang, J., Cao, Y., Wang, Z., Zhang, G., Hou, D., 2023. River surface velocimetry based on virtual river dataset and modulated-RAFT. IEEE Access 11, 38275–38290. https://ieeexplore.ieee.org/abstract/document/10103463/.
- Xu, Q., Fan, X.-M., Huang, R.-Q., Westen, C.V., 2009. Landslide dams triggered by the Wenchuan Earthquake, Sichuan Province, south West China. Bull. Eng. Geol. Environ. 68, 373–386. https://doi.org/10.1007/s10064-009-0214-1.

- Xu, W.-J., Xu, Q., Wang, Y.-J., 2013. The mechanism of high-speed motion and damming of the Tangjiashan landslide. Eng. Geol. 157, 8–20. https://doi.org/10.1016/j. enggeo.2013.01.020.
- Yang, L., 2023. Analysis on instability mechanism and influencing factors of Baige Landslide on Jinsha River. Yangtze River 54, 1–7 (in Chinese).
- Yang, S.Q., Lim, S.Y., 1997. Mechanism of energy transportation and turbulent flow in a 3D channel. J. Hydraul. Eng. 123, 684–692. https://doi.org/10.1061/(ASCE)0733-0439(10071)3-96840
- Yang, S.-Q., Lim, S.-Y., 1998. Boundary shear stress distributions in smooth rectangular open channel flows. ICE Proc. Water Marit. Energy 130, 163–173. https://doi.org/ 10.1680/iwtme.1998.30975.
- Yang, Y., Chen, G., Meng, X., Chong, Y., Shi, W., Bian, S., Jin, J., Yue, D., 2024. Characteristics of the impact pressure of an outburst debris flow: insights from experimental flume tests. Eng. Geol. 330, 107428. https://www.sciencedirect.com/ science/article/pii/S0013795224000267.
- Yin, Y., 2000. Study on characteristics and disaster reduction of giant landslide in Yigong, Bomi, Tibet. Hydrogeol. Eng. Geol. 27, 8–11 (in Chinese). http://qikan.cqvi p.com/Qikan/Article/Detail?id=4280958.
- Yu, B., Yang, C., Yu, M., 2022. Experimental study on the critical condition of river blockage by a viscous debris flow. Catena 213. https://doi.org/10.1016/j. catena.2022.106198.
- Zeng, P., Wang, S., Sun, X., Fan, X., Li, T., Wang, D., Feng, B., Zhu, X., 2022. Probabilistic hazard assessment of landslide-induced river damming. Eng. Geol. 304. https://doi. org/10.1016/j.enggeo.2022.106678.
- Zhang, Q.-Z., Qing, P., Ying, C., Ze-Jun, L., Zhen-Ming, S., Yuan-Yuan, Z., 2019. Characteristics of landslide-debris flow accumulation in mountainous areas. Heliyon 5, e02463. https://www.ncbi.nlm.nih.gov/pubmed/31687562.
- Zhang, J.-Y., Fan, G., Li, H.-B., Zhou, J.-W., Yang, X.-G., 2021. Large-scale field model tests of landslide dam breaching. Eng. Geol. 293. https://doi.org/10.1016/j. enggeo.2021.106322.
- Zhang, J.-Y., Yang, X.-G., Fan, G., Li, H.-B., Zhou, J.-W., 2023. Investigating the important role of landslide dam geometry on breaching based on numerical experiments. Eng. Geol. 323. https://doi.org/10.1016/j.enggeo.2023.107210.
- Zhong, Q., Wang, L., Chen, S., Chen, Z., Shan, Y., Zhang, Q., Ren, Q., Mei, S., Jiang, J., Hu, L., Liu, J., 2021. Breaches of embankment and landslide dams - state of the art review. Earth Sci. Rev. 216. https://doi.org/10.1016/j.earscirev.2021.103597.
- Zhou, G.G.D., Zhou, M., Shrestha, M.S., Song, D., Choi, C.E., Cui, K.F.E., Peng, M., Shi, Z., Zhu, X., Chen, H., 2019a. Experimental investigation on the longitudinal evolution of landslide dam breaching and outburst floods. Geomorphology 334, 29–43. https://doi.org/10.1016/j.geomorph.2019.02.035.
- Zhou, Y., Shi, Z., Zhang, Q., Jang, B., Wu, C., 2019b. Damming process and characteristics of landslide-debris avalanches. Soil Dyn. Earthq. Eng. 121, 252–261. https://doi.org/10.1016/j.soildyn.2019.03.014.
- Zhou, Y., Shi, Z., Zhang, Q., Liu, W., Peng, M., Wu, C., 2019c. 3D DEM investigation on the morphology and structure of landslide dams formed by dry granular flows. Eng. Geol. 258. https://doi.org/10.1016/j.engeo.2019.105151.
- Zhou, G.G.D., Li, Š., Lu, X., Tang, H., 2022a. Large-scale landslide dam breach experiments: overtopping and "overtopping and seepage" failures. Eng. Geol. 304. https://doi.org/10.1016/j.enggeo.2022.106680
- https://doi.org/10.1016/j.enggeo.2022.106680.

 Zhou, G.G.D., Lu, X., Xie, Y., Cui, K.F.E., Tang, H., 2022b. Mechanisms of the Non-uniform breach morphology evolution of landslide dams composed of unconsolidated sediments during overtopping failure. J. Geophys. Res. Earth 127. https://doi.org/10.1029/2022.JF006664.
- Zhou, X., Zhou, J., Du, X., Chen, Z., 2022c. Emergency rescue and disposal technology for Baige Barrier Lake on the Jinsha River, China. In: Zhou, X., Zhou, J., Du, X., Chen, Z. (Eds.), Scientia Sinica Technologica, pp. 343–356 (in Chinese). https://www.sciengine.com/doi/pdf/7EA342FA40EA477597EF6DAE9C2590EB.
 Zhou, Y., Shi, Z., Qiu, T., Zheng, H., 2022d. Failure characteristics of landslide dams
- Zhou, Y., Shi, Z., Qiu, T., Zheng, H., 2022d. Failure characteristics of landslide dams considering dam formation features in laboratory experiments. Landslides. https:// doi.org/10.1007/s10346-022-01907-6.
- Zhu, Q.-Y., Jiang, N., Chen, Q., Hu, Y.-X., Zhou, J.-W., 2023. DEM-SPH simulation for the formation and breaching of a landslide-dammed lake triggered by the 2022 Lushan earthquake. Landslides. https://doi.org/10.1007/s10346-023-02096-6.